PRISM: Practical Design and Orchestration of Frequency-Shifting RIS for NLoS mmWave Sensing

Aadesh Madnaik, Karthikeyan Sundaresan

School of Electrical and Computer Engineering, Georgia Institute of Technology

Abstract

Millimeter wave (mmWave) radar sensing is essential for Integrated Sensing and Communication (ISAC) but is limited by the need for line-of-sight (LoS) in environments with obstacles. However, existing non-line-of-sight (NLoS) solutions, including those leveraging reconfigurable intelligent surfaces (RIS) are computationally demanding, unable to generalize to new surroundings or require tight synchronization/coordination that prevent practical deployments. We propose PRISM, a framework that brings the diversity of a RIS to monostatic radars to enhance target resolution in NLoS, all without requiring real-time coordination. PRISM uses spatial modulation at the RIS to encode targets' angular information through frequency shifts by creating a time-variant channel for improved detection at the radar. Key contributions include a wideband spatial modulation framework, a genetic algorithm to efficiently solve for the RIS configuration to enable such angle-dependent frequency shifts, and a narrowband approximation method to reduce the computational overhead. Evaluations show PRISM benefits chirp-based radars by reducing mean localization error to 31 cm and maintaining 80% target detection accuracy for up to six targets in NLoS compared to 103 cm error and 66% accuracy with prior art, while providing a 12x reduction in computation time.

Keywords

Reconfigurable Intelligent Surfaces, Metasurface, mmWave, radar

1 Introduction

Integrated Sensing and Communication (ISAC) systems have emerged as a key paradigm in 5G/6G systems, aiming to unify radar sensing and wireless communication on a shared infrastructure [1]. For example, dual-function radar-communication (DFRC) systems [2, 3] leverage shared waveforms—such as chirp or FMCW—and common hardware to perform both sensing and communication tasks simultaneously, thereby improving spectral and hardware efficiency. However, both mmWave communication and sensing are limited by the crucial requirement of line-of-sight (LoS), i.e., a direct path between the radar and the target, for several applications [4, 5]. Fig. 1 illustrates a practical indoor deployment where the presence of walls and narrow corridors is unavoidable. Particularly for a sensing system, limiting the maximum detection area solely to LoS (area colored in blue) decreases its utility and makes the need to sense targets around corners (area colored in red) more pressing. To bridge this gap, we propose a practical approach leveraging reconfigurable intelligent surfaces (RIS) to enhance NLoS sensing, thereby enabling more robust ISAC solutions.

In the past, several data-driven solutions have been proposed to localize non-line-of-sight (NLoS) targets using the radar's coarse point cloud [6–8]. These solutions fall short of practical deployment due to increased computational requirements, inaccuracies in environmental modeling, and the inherently limited spatial resolution of
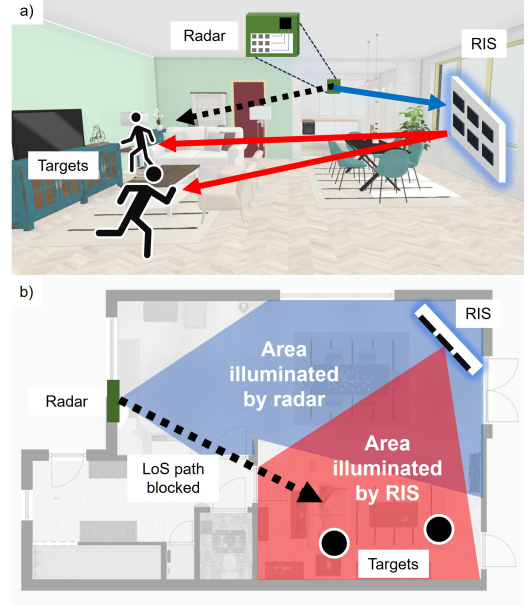

Figure 1: An illustration of a) orthographic projection of a typical system setup, b) top-view of system setup

the radar. The root cause of problems in indoor deployments is the seemingly uncontrollable multipath propagation which creates unpredictable pseudo-targets in the radar's point cloud confounding the detection of true targets as illustrated in Fig. 3.

Reconfigurable Intelligent Surfaces (RIS) are a promising paradigm for controlling signal propagation paths within the environment. Most prior work involving RIS has focused on improving communication capabilities [9–12]. In contrast to communication systems that are naturally bistatic (active transmitter and receiver), practical mmWave sensing is accomplished using monostatic radar signal processing. For monostatic radar sensing to benefit from RIS reflections, the latter must be capable of conveying the angular information of the targets. This is often achieved by the impractical assumption of tight synchronization and coordination between radar and the RIS, allowing the radar to configure and know the beam employed by the RIS at any instant. On the other hand, when such a stringent requirement is eliminated, the angular information of the reflected signals from the RIS corresponding to different targets can no longer be differentiated. This poses a fundamental challenge in leveraging RIS and its reflections for practical monostatic radar sensing, forming our focus in this work.

To effectively aid monostatic radar sensing, the RIS-based deployment must meet several key requirements: (1) RIS must preserve angular information for multiple targets simultaneously; (2) RIS should be easily integrated into the existing chirp-based range-Doppler analysis used by radars which would allow for seamless

adoption into the system's signal processing pipeline; (3) RIS configurations should not require real-time coordination with the radar system. This independence simplifies the system design and reduces the need for complex synchronization mechanisms, making RIS a more viable solution for enhancing monostatic radar sensing capabilities in real-world deployments.

In this work, we introduce PRISM, a *P*ractical *RIS*-based sensing solution that employs *S*patial *M*odulation to provide robust angular resolution in high multipath indoor environments without the need for line-of-sight. Our passive methodology integrates a RIS into a commodity radar's sensing framework without modifying its signal processing pipeline. At the heart of PRISM is a spatial modulation framework for RIS that is readily compatible with any chirp-based radar, offering enhanced angular resolution of targets without requiring coordination between radar and RIS. The spatial modulation approach leverages the wide bandwidth intermediate frequency (IF) processing of radars to encode the target's angular information through *frequency-shifts* by the RIS (Fig. 2). By varying the phase configuration of the RIS elements with a pre-defined sequence at the order of several MHz, PRISM creates a controlled *time-variant* channel between several targets and the radar through the RIS. When the radar's signal, reflected from the targets, propagates through this time-variant channel, it undergoes shifts in frequency that are dependent on its incoming angle. This allows the RIS to encode the angular information of targets in the IF spectrum of the signal reflected by it, allowing the radar to leverage its existing IF processing techniques to isolate reflections from the environment from those from the RIS. In essence, through the spatial modulation framework, the RIS serves as distributed antenna elements of the monostatic radar, seamlessly preserving the angular information of targets while remaining robust across different environments, thereby improving target resolution capabilities beyond those of the radar itself.

Our contributions to the design of PRISM are three-fold: (1) a novel, general-purpose, wideband spatial modulation framework for frequency-shifting RIS that can be leveraged by monostatic radars (commodity or DFRC systems); (2) a genetic algorithm to solve for the RIS configurations; and (3) a narrowband approximation to accelerate computation. The spatial modulation framework helps provide an accurate model to build the desired time-variant channel and realize the frequency shifting effect with RIS that works seamlessly with radars. However, obtaining the corresponding space-time configurations that need to be applied to the RIS to realize the desired frequency-space profile over the wide bandwidth of the radar signal remains a challenging problem because of its non-convex and high dimensional structure. We propose a narrow-band approximation of the wideband problem that allow us to efficiently solve it by instrumenting a genetic algorithm to suit the nuances of space-time modulation, while incurring an order of magnitude lower complexity compared to its wideband counterpart.

PRISM is extensively evaluated in real indoor environments whose multipath channels are measured using a 5G FR2 (39 GHz) testbed running an OAI stack [13] spanning both LoS and NLoS layouts with varying number of targets. We supplement our evaluations with multipath channels generated using Wireless InSite [14] for indoor and outdoor deployments. Our evaluations highlight that PRISM benefits radars with a 3.3x reduction in mean localization
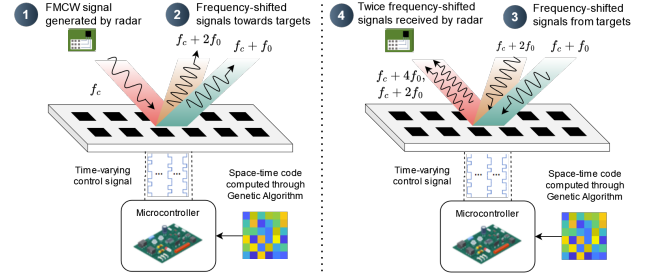
Figure 2: Conceptual illustration of two-way signal propagation in a frequency-shifting RIS

error to 31 cm and maintains 80% target separation accuracy for up to six targets in NLoS compared to 103 cm error and 66% accuracy with prior art. Further, its increased spatial/angular resolution also benefits LoS with superior multi-target target resolution capability (F_1-score over 0.9) – all while reducing the computation time by 12x without sacrificing on the target detection accuracy. PRISM's practical approach allows commodity radars of today to readily benefit from RIS in NLoS sensing.

2 Background & Motivation

2.1 Background & Related Work

In the past, several solutions have been proposed to overcome challenges associated with sensing NLoS targets.

2.1.1 Ray tracing approaches. The process of ray tracing relies on the ability to effectively model the geometry of the space as well as the reflections off walls. Several works [15–19] resort to heuristics to identify the targets or use methods that often assume ideal environmental conditions, such as minimal multipath interference and predictable geometrical configurations of the environment, which limit their applicability in complex indoor settings. Advanced ray tracing algorithms improve accuracy but come at the cost of increased computational complexity and the need for detailed environmental modeling.

2.1.2 Learning-based approaches. These approaches [6, 20] leverage machine learning models to interpret radar signals and predict target locations. While promising, these methods fail to adapt to scenarios not included in the training dataset. Furthermore, the spatial resolution of these models is fundamentally limited by the radar's capabilities since the data obtained is radar-specific. Additionally, models trained on data from high-resolution radars do not generalize well to radars with poorer resolution, making the approach less flexible.

2.1.3 RIS-based approaches. Augmenting the environment with reflectors in known locations is a popular choice since it provides an additional dimension of information, thus offering a more predictable and robust solution than learning-based approaches. Within the class of solutions based on reflectors, there are two categories: (1) passive reflectors (metasurfaces); and (2) RIS which are low-cost reconfigurable surfaces.

In the category of passive reflectors, [21] employs a multi-reflector setup with a gray-code to encode the angle of reflection. However, [21] faces several limitations in indoor scenarios since the non-orthogonal coding depends on a strong and singular path between

the reflectors and the target. Relying on peak detection for target identification becomes problematic when multiple targets and multipath reflections are present, which are common occurrences in indoor environments, as we show in evaluations. Furthermore, passive reflectors need to be designed for specific scenarios.

In contrast, a RIS is inherently reconfigurable, enabling it to adapt to various environments and applications, including both sensing and communications. However, integrating a RIS into a mmWave sensing setup, especially with chirp-based radars, remains challenging. Prior solutions [22–30] involve an active RIS and/or fine-time synchronization between the RIS and radar hardware to actively reconfigure the RIS elements, a capability that is impractical to realize with DFRC systems since it creates significant overheads in both, spectral and temporal resources. Furthermore, some of the aforementioned solutions involving MIMO and dual-function radar-communication (DFRC) systems, necessitates the use of sophisticated signal processing and/or the complete redesign of the transmitted waveform which decreases compatibility with the 5G mmWave standard. In contrast, our proposed solution is compatible with commonly-deployed chirp-based radar hardware since it utilizes a passive spatial modulation framework at the RIS, which eliminates the need for synchronization and coordination between the radar and the RIS and dedicated MIMO/DFRC hardware.

2.2 Limitations in NLoS Sensing with RIS

In this section, we consider the requirements of a practical NLoS scenario with a radar and several targets as illustrated in Fig. 3. As discussed previously, augmenting such NLoS environments (i.e. no direct path between the radar and targets) with a RIS is a favourable choice. To avoid real-time coordination and synchronization between radar and RIS, we consider a practical solution that employs a wide-beam configuration at the RIS to redirect electromagnetic energy from a desired area of coverage (targets) to the radar. Fig. 3a illustrates the aggregate spectrogram received at the radar using CIRs extracted from Wireless InSite [14], showcasing significant ambiguity in the resolution of 3 targets from the radar's range profile. This can be attributed to two key factors: (i) lost angular (azimuth) information of targets in RIS' reflections, and (ii) increased impact of multipath. The inability to coordinate and synchronize at fine time scales with radars, prevents RIS from having narrow beams since they can miss important target reflections. The resulting drawback is both lost angular resolution of targets (closely spaced targets appear indistinguishable) as well as reduced multipath suppression capability (desired target reflections confounded by reflections from walls, furniture, etc.).

In summary, the key requirements of a RIS to aid in practical NLoS sensing by a chirp-based radar are: (1) the ability to resolve the angles of arrival of signals incoming from several directions simultaneously; (2) enable beamfornming for effective multipath suppression; (3) no active dependence on time synchronization or communication between the radar and RIS; and (4) integrate seamlessly into the radar's signal processing pipeline.

2.3 Key Idea: Frequency-Shifting RIS

As a core contribution, our approach delivers on the promise of NLoS sensing by addressing the critical challenge of preserving
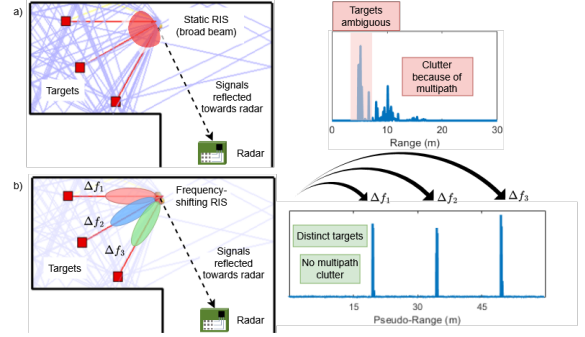
Figure 3: Simulating the presence of three targets and one passive reflector. The propagation paths and CIRs were extracted from Wireless InSite.

angular resolution of targets at the RIS along with multipath suppression without requiring an active communication link or synchronization with the radar. We employ a novel spatial modulation technique which encodes the angle-of-arrival of incident signals at the RIS into the frequency domain by *frequency-shifting* based on spatial cues. By varying the RIS configuration deterministically at the order of several MHz, we are able to shift signal frequency and beamform in several directions simultaneously towards the targets as seen in Fig. 2. This enables both beamforming (multipath suppression) and preservation of target angular information at the RIS, while the space-time configurations are locally applied at the RIS without any real-time coordination with the radar, enabling practical deployments. The shift in frequency of the RIS-reflected signals translates to a *pseudo*-range of 10s of meters in the radar's range-doppler profile, which is sufficiently more than the practical range of the radar, allowing for easier differentiation of the RIS-reflected signals from the LoS reflections, while allowing for seamless integration with radar's existing processing pipeline.

Fig. 3b illustrates an anecdotal deployment of a frequency-shifting RIS. With the help of spatial modulation, the RIS was configured to create frequency shifts of 2, 4, and 6 MHz for beamforming (with a beamwidth of 15°) in the directions of targets 1, 2, and 3 simultaneously. Since 2 MHz corresponds to a range offset of 15 meters (one-way) on the radar's range profile (much larger than typical operational range), the $x-$axis stretches to span 60 meters. Appearing distinctly within the ranges of $[15, 30]$, $[30, 45]$, $[45, 60]$ meters respectively, we see 3 sharp and singular peaks, indicating that the direct path (colored red) between the target and the RIS has been isolated from the other reflected paths (colored blue).

3 PRISM Design

3.1 PRISM Overview

The design and operation of PRISM is illustrated in Fig. 4.

Configuring the RIS: The first step to making the system operational is to determine the desired mapping of frequency shifts to angles-of-arrival at the RIS, i.e., the frequency-space encoding, $\mathbf{G}^*$. Sections 3.2 and 4 describe how a time-varying RIS configuration, named space-time code, satisfies the functionality of a frequency-space encoding. The space-time code can be locally applied at the RIS in an environment-agnostic manner since the wider aperture isolates multipath effects, all without coordination with the radar.
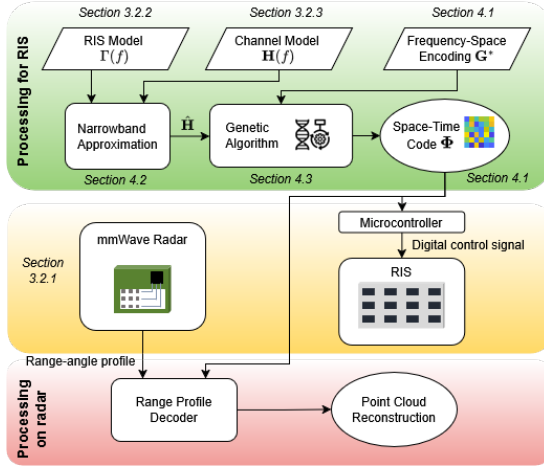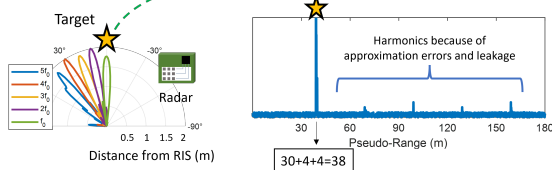
Figure 4: Overview of PRISM

Figure 5: RIS-reflected targets in the range profile of FMCW radars capturing forward and backward paths

Our primary objective is to determine the best space-time code that allows the RIS to create the desired frequency-space encoding. Since this requires solving a non-linear objective function, we propose an optimization framework based on genetic algorithm which determines the most suitable RIS configuration. This space-time code, Φ^*, is then programmed into the RIS (one-time), allowing it to create the desired frequency-space encoding in its reflected signals without requiring any real-time coordination with the radar, thereby facilitating practical deployments. To accommodate the wide bandwidth (e.g. 1-4 GHz) of mmWave radars, the objective function used in the genetic algorithm is based on a wideband integral formulation, which is computationally challenging. To minimize computational overheads, we approximate the wideband channel with a narrowband channel, which we analytically characterize to be of minimal error through Theorem 4.1.

Seamless RIS Operation with Radar: During operation, the RIS executes the space-time code as a periodic, time-varying voltage signal switching the phases of its elements, without any real-time coordination with the radar. In a typical FMCW (chirp) radar, after dechirping (described later in Section 3.2) and applying a Fourier transform to received signals, the radar observes several beat frequencies. These frequencies correspond to discrete peaks in the range profile, where each peak corresponds to a potential target at a specific range. However, when a signal is incident on the RIS, the latter's angular modulation induces frequency shifts (i.e. harmonics of f_0) as a function of the incidence angle in the reflected waves. With f_0 chosen such that RIS-reflected signals occupy a range profile larger than the typical operational range of radars (e.g. f_0 =
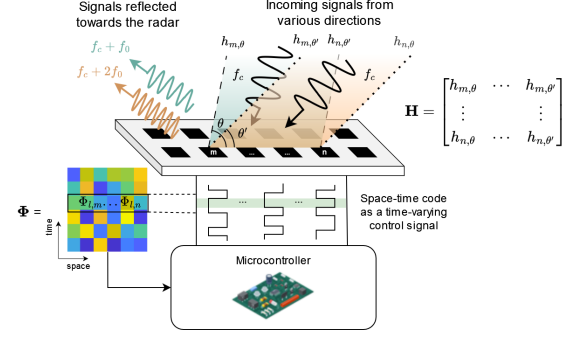

Figure 6: Principle of operation of a frequency-shifting RIS

2 MHz corresponds to 15 m), the radar can easily distinguish the AoA of signals from the RIS and accordingly account for the impact of RIS for seamless target detection even in NLoS settings using radar's existing processing pipeline. As an example, consider an object in NLoS that is 2 m away and at 0° (normal) from RIS, and the radar is pointing towards the RIS from 2 m away at −45°, as seen in Fig. 5. The RIS encodes the signals in harmonics of 2 MHz for every 12°. The signal is reflected off the RIS twice (forward and backward paths); thus, corresponding to 0°, we get a peak between 30 and 60 m (an object at 12° would map to the range bin 60-90m). With the total path length through RIS being 8 m (2m between radar-RIS), a peak appears at a distance of 38 m, revealing a target at an angle of 45° and a distance of 2 m from the RIS.

3.2 PRISM Model

There are three main entities in PRISM as illustrated in Fig. 1: 1) a mmWave radar, 2) the RIS, and 3) targets.

3.2.1 FMCW Radar Model. A typical mmWave radar transmits an FMCW waveform and infers the location of the targets from the reflected signals. 3D point clouds are obtained and processed at the radar by extracting the range, azimuth and elevation information encoded in the received signal. In FMCW radars, the difference in frequencies of the transmitted and received signals is used to find the signal propagation time, and thus the range and when applied at a slow timescale across chirps, also reveals doppler [31, 32].

Our proposed solution exploits the fact that the radar infers the range indirectly through the frequency of the received signal rather than measuring time-of-flight itself. With a frequency-shifting RIS, we propose inducing a frequency shift in the signals, thereby adding to the distance of the object in a deterministic manner. The induced frequency shift is greater than realistic distances in indoor settings which enables the radar to identify real ranges from *pseudo*-ranges.

3.2.2 RIS Model. A typical RIS consists of a large number of tiny reflectors placed in a two-dimensional planar array as illustrated in Fig. 6. With the help of a low-cost microcontroller, the reflection phases of each of these patch elements can be controlled independently. Commonly, the reflection coefficient of an element indexed n is modeled as a phase change of $\Phi_n = e^{j\varphi_n}$ [9, 10].

Furthermore, the most prevalent patch antenna element designs employed by RIS do not have a uniform reflection coefficient across the operating frequency band [33]. Since commodity mmWave radars operate over a large bandwidth (1-4 GHz), in our analysis

we denote the frequency-dependent reflection coefficient (S_{11} parameter) of a patch antenna element with the function $\Gamma(f)$. The functional form of the reflection coefficient is more general than a communication-oriented subcarrier approach [34, 35]. For our simulations, we consider the wideband reflection coefficient of a rectangular patch antenna on a Rogers RO4350B substrate simulated in COMSOL.

Accurately modeling the combined effect of phase shifting and the wideband reflection coefficient is instrumental in deciding the configuration of the RIS (further discussed in Section 4).

3.2.3 Channel Model. We present the channel model of PRISM using geometrically-dependent paths. Note that the channel model's role is to capture the RIS' array pattern and hence depends only on its structure and not on the environment, thereby requiring *no explicit estimation.* Like other beamforming works, our model considers the far-field channel approximation of uniformly spaced RIS elements. For a linear array with inter-element spacing d_x, and a target at azimuth θ, we can simplify the relationship between the channels from elements indexed n and 1 as (see Fig. 2),

$$h_{n,\theta}(f) = h_{1,\theta}(f) \exp\left\{-j\frac{2\pi f}{c}\left[(n-1)d_x\sin\theta\right]\right\}. \quad (1)$$

We validate the far-field channel model using channel traces collected from our testbed and verify that the strongest path follows Eq. 1. However, there is an additional layer of complexity: the complex propagation channels are frequency, f, dependent. When the bandwidth of operation is large , the channel coefficients vary drastically across the operating band. The large variation in channels creates the well-known problem of beam-squinting which makes it challenging to provide consistent gain in wideband systems compared to conventional narrowband systems. To account for the wideband nature, we propose a model and corresponding loss function in Section 4.1.2 structured as a matrix-integral over the bandwidth of operation.

While a radar signal is reflected by the RIS in both directions (radar-RIS-target, target-RIS-radar) in a NLoS setting (Fig. 2), let us consider the return path (target-RIS-radar) from a target (say, at angle θ) for easier exposition. Each of these paths can be modeled as a product of the channel between the target and the RIS element, the reflection phase of the element, Φ_n, and the channel between the element and the radar. Since the positions of the radar and the RIS are fixed, without loss of generality, we can condense the notation of the aggregate wideband channel into a summation. The aggregate channel, $h_\theta(f)$, is a superposition of all the individual propagation paths, given as

$$h_\theta(f) = \sum_{n=1}^{N} \Phi_n \Gamma(f) h_{n,\theta}(f).$$

Communication-centric objectives like improving the signal strength or nulling interference in a particular direction can be achieved through a suitable choice of Φ_ns, i.e. controlling the phase of the RIS elements. Similarly, we will define an appropriate objective for NLoS sensing with radars.

4 Spatial Modulation Framework

First, we introduce the theory of spatial modulation related to reconfigurable intelligent surfaces. In particular, we detail how a time-varying configuration satisfies the simultaneous requirement of frequency-shift and beamforming demanded by the mmWave radar. However, finding the optimal time-varying configuration is non-trivial and demands significant computational resources. Therefore, we present an efficient approximation approach aimed at simplifying the objective function without sacrificing performance. Lastly, we propose an optimization framework based on genetic algorithm that minimizes the objective function while incorporating the intricacies and constraints of operating a RIS.

4.1 Spatial Modulation

The overarching goal of spatial modulation in RIS is to create a frequency-space profile, i.e., to effect a deterministic frequency shift in a particular direction as illustrated in Fig. 6. The frequency-space profile, $\mathbf{G}^* \in \{0, 1\}^{M \times |\Theta|}$, is a binary matrix mapping the angles of incidence on the RIS to the the shift in frequency the RIS creates. The directions in consideration are a finite set of angles such as $\Theta = \{-90°, -80°, \cdots, 90°\}$, and the shifts in frequency are a set of pre-determined harmonics like $\{f_0, \cdots, Mf_0\}$.

It is not possible to shift frequencies using static RIS elements since the channel remains time-invariant. In order to shift frequencies and beamform in several directions simultaneously, we must create a *controlled, time-variant channel* between the targets and the radar. We vary the complex channel in phase through the application of a periodic control signal to each of the RIS elements which results in a frequency-space profile. The control signal changes the complex phase, Φ, of the RIS elements. The periodic nature of the control signal ensures that only harmonic frequencies are excited. We divide the period, T, into L time-slots where we assign a complex phase for each of the N elements as $\Phi = \left[\Phi_{l,n}\right] \in \{\pm 1, \pm j\}^{L \times N}$. This matrix is termed 'space-time code' since it varies the configuration of the RIS based on element (space), n, and (time) slot, l. For the sake of brevity, we omit details pertaining to time-domain analysis of space-time codes. While [36, 37] explore time-domain analysis in more detail, they do not consider wideband analysis, which is central to mmWave radars and in turn forms our focus.

4.1.1 Problem setup. To analytically quantify the overall channel, we create a matrix, $\mathbf{H}$, of the complex channel coefficients evaluated as $\mathbf{H} = \left[h_{n,\theta}\right] \in \mathbb{C}^{N \times |\Theta|}$ using Equation 1. The rows represent the variation of the complex channel with the element indices, n, while the columns represent the variation with azimuth angle, θ. Recall that $\mathbf{H}$ is environment-agnostic and captures the RIS' array structure that influences the space-time code needed to achieve the desired frequency-space profile. Signals from several targets come in from several unique angles towards the RIS. Based on the angle of incidence, θ, and the configuration of the RIS, Φ, in that particular timeslot, l, the incident signal undergoes a multiplicative transformation. The multiplicative factor is the overall *time-varying* channel through the RIS. This l- and θ-dependent scalar is the sum over the individual channels of the RIS elements and can be stacked into a matrix.

$$\left[\textstyle\sum_n \Phi_{l,n} h_{n,\theta}\right] = \Phi\mathbf{H} \in \mathbb{C}^{L \times |\Theta|}$$
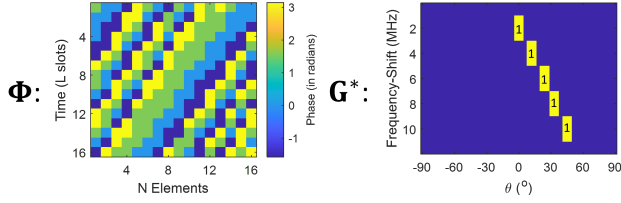
Figure 7: Space-time code resulting in frequency shifts of $f_0 = 2$ MHz

The time-varying channel is periodic with time period T, so we observe harmonics at multiples of the fundamental frequency $f_0 = 1/T$, each of which corresponds to a different θ. We would like to quantify the amplitude gain created by the space-time code for a harmonic multiple mf_0 for an angle of incidence θ. Through Fourier transformation, we obtain the frequency domain representation of the time-varying channel. It quantifies the shift in frequency created, that can be evaluated as

$$\mathcal{F}_T \left\{ \left[\sum_n \Phi_{l,n} h_{n,\theta} \right] \right\} = \mathbf{W\Phi H} \qquad (2)$$

where $\mathbf{W}$ is matrix representation of the Fourier transform of a periodic, piecewise-defined function[1]. For an incident RF signal, the radar receives several frequency-shifted versions which are scaled corresponding to the entries in Equation 2.

For instance, consider the space-time code illustrated in Fig. 7. The RIS in consideration has 16 elements. The period, $T = 500$ ns, is split into 16 time-slots. For a configuration where each of the RIS elements is in one of the states $\{\pm 1, \pm j\}$, we observe harmonics of the fundamental frequency $f_0 = 1/T = 2$ MHz. This particular RIS configuration (Fig. 7a) modulates the incident wave differently for each of the angles $\{0°, 11°, 22°, 34°, 45°\}$ onto the different harmonics (Fig. 7b). The strongest components of the frequency shift are in multiples of the base frequency. It is also notable that this is a good configuration since there is minimal leakage of energy into other directions for any of the beams. While this example considers only the return path, in a NLoS setting with two-way reflections through the RIS, the frequency shifts are exactly doubled as shown in Fig. 2.

4.1.2 Defining the Objective Function. The modulation creates a dynamic but controlled propagation environment for the mmWave signals. Critically, we also observe that there is a frequency-dependence in the amplitude of the modulating wave. Hence, we must redefine the objective problem to better suit wideband operation in the context of spatial modulation.

We argue that amplitude by itself is an insufficient measure of the beam pattern. More robustly, the cumulative gain in spectral energy content is a more suitable measure for the beam pattern. The total gain in energy carried by the modulating waveform is the element-wise integral over the bandwidth $[f_A, f_B]$ defined as

$$\mathbf{G}(\Phi) = \frac{1}{f_B - f_A} \int_{f_A}^{f_B} \|\mathbf{W\Phi H}(f)\|^2 df. \qquad (3)$$

The effective channel matrix is defined as $\mathbf{H}(f) = \left[h_{n,\theta}(f)\Gamma(f) \right]$ to accomodate for the frequency response of the antenna elements.

---

[1]Elements of the Fourier transform matrix of a periodic, piecewise-defined function can be derived as $W_{nl} = \frac{\exp\{-j2\pi n(l-1)/L\} - \exp\{-j2\pi nl/L\}}{j2\pi n}$.

The matrix of beam energies, $\mathbf{G}(\Phi)$, encapsulates both, the angle in which the incident wave is reflected and the frequency with which the beam is modulated.

Our formulation defines a mapping from the choice of a space-time code, Φ, to the resulting wideband beam pattern, $\mathbf{G}(\Phi)$. We establish a global optimization framework which is tasked to obtain the desired beam pattern $\mathbf{G}^*$ by minimizing the Frobenius norm of the difference between the desired and estimated beam patterns.

$$\Phi^* = \underset{\Phi \in \{\pm 1, \pm j\}^{L \times N}}{\arg \min} \|\mathbf{G}^* - \mathbf{G}(\Phi)\|_F \qquad (4)$$

4.2 Efficient Approximation of Wideband Operation

To solve the optimization problem, the solver must search over the entire space of possible space-time codes. The solution space grows exponentially with the size of the RIS and the number of time-slots in the space-time code. For example, if the RIS is a 16-element array, 2-bit controllable, and there are 16 time slots, there are $4^{256} \approx 1.3e154$ possible distinct patterns. Additionally, computing the objective function itself is a hard and inefficient problem since it involves evaluating at least 256 integrals in each step.

There are several sub-optimal ways to approximate the integral formulation. For instance, one could partition the interval into discrete units (like a Riemann integral [38]) and evaluate the aggregate. To get a good approximation, the bandwidth must be divided into several sub-intervals, which scales poorly for large bandwidths. Additionally, making the naive assumption that the best approximation of the channel matrix in Equation 5 is the arithmetic mean itself, i.e. averaging the channel coefficients over the entire bandwidth, is a poor choice as seen in Section 5. While averaging might work for narrow bandwidths, the assumption does not hold for larger bandwidths where the mapping from Φ to $\mathbf{G}$ is non-linear.

In order to make a more robust approximation while keeping the order of computational overhead low, we propose approximating the wideband integral in Equation 5 with a spectral energy equalized channel ($\hat{\mathbf{H}}$) as defined in Theorem 4.1.

$$\hat{\mathbf{G}}(\Phi) = \|\mathbf{W\Phi\hat{H}}\|^2 \approx \frac{1}{f_B - f_A} \int_{f_A}^{f_B} \|\mathbf{W\Phi H}(f)\|^2 df. \qquad (5)$$

THEOREM 4.1. *Given a matrix of functions* $\mathbf{H}(f) = \left[\mathbf{h}_1(f), \cdots, \mathbf{h}_P(f) \right]$, *its matrix approximation with the least expected error is* $\hat{\mathbf{H}} = \left[\hat{\mathbf{h}}_1, \cdots, \hat{\mathbf{h}}_P \right]$ *where* $\forall p, \hat{\mathbf{h}}_p$ *can be evaluated by applying Lemma A.1 on* $\mathbf{h}_p(f)$.

Lemma A.1 states that the narrowband approximation with least expected error, $\hat{\mathbf{h}} \in \mathbb{C}^N$, of any wideband channel vector, $\mathbf{h}(f) \in (L^2)^N$, is the best rank-1 approximation of $\mathbf{h}(f)$'s auto-correlation matrix as defined by Equation 10.

Following this approximation step, we propose to minimizing a new objective function as defined in Equation 7 that is equivalent to solving Equation 4 to obtain the desired space-time configuration.

$$\Phi^* = \underset{\Phi \in \{\pm 1, \pm j\}^{L \times N}}{\arg \min} \underbrace{\|\mathbf{G}^* - \mathbf{G}(\Phi)\|_F}_{\text{difficult to compute}} \qquad (6)$$

$$\approx \underset{\Phi \in \{\pm 1, \pm j\}^{L \times N}}{\arg \min} \underbrace{\|\mathbf{G}^* - \hat{\mathbf{G}}(\Phi)\|_F}_{\text{easy to compute}} \qquad (7)$$
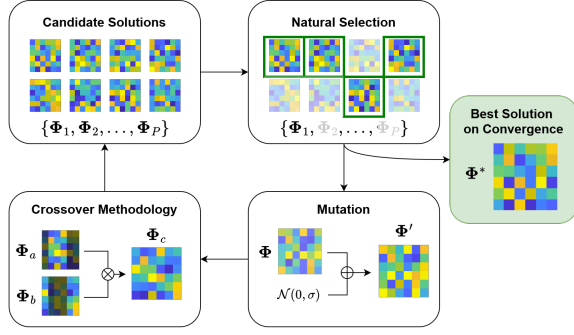
Figure 8: Illustration of GA pseudo-code

4.3 Solving with Genetic Algorithm

While easier to compute, the objective function defined in Equation 7 is still high-dimensional and non-convex. Constrained by the 2-bit quantization of the RIS, the solution space of the problem has been appropriately discretized. This condition curbs the kind of solvers we can use to find the optimal solution. We cannot use Moore–Penrose inversion [39] of the matrices since they are used to compute least-squares solutions which can lie anywhere in the complex domain. Additionally, we cannot use gradient-descent since the problem is non-convex and the domain itself is discontinuous. The constraints and formulation of the problem places it squarely in the territory of *global optimization problems without an analytic solution*. A widely-recognized solution methodology to such hard problems is the class of genetic algorithms. They are inspired by the process of natural selection, mutation, crossover, and fitness, all of which are stochastic models.

We now instrument the four primary steps of the genetic algorithm (illustrated in Fig. 8) and tailor it to our RIS problem.

4.3.1 Candidate solutions. The genetic algorithm works with a large set of candidate solutions/configurations. The phase configuration of the RIS is discrete and complex. However, discrete domains can create problems with fast-convergence for the class of genetic algorithms. Hence, we model the RIS configuration for each element n in time-slot l as a mapping from the real domain to phase-wrapped, unit-magnitude complex domain ($\Phi = \left[e^{jx_{nl}} \right], x_{nl} \in \mathbb{R}$). Following this, we map the idealized phase (continuous) to a more realistic phase (2-bit discretized) by choosing the nearest neighbor. We initialize the set of candidate solutions (unique $N \times L$ dimensional vectors) with a population size of 100. The vectors in the set are picked randomly with a normal distribution.

4.3.2 Natural Selection. First, the algorithm evaluates the 'fitness' of each of the candidate solutions with the objective function described in Equation 4 and approximated by Equation 7. The smaller the value of the objective function, the more 'fit' a solution is. In the natural selection step, the fitness of all candidate solutions is evaluated. Only the top 50% of candidates are preserved, while the lower half, i.e. the least-fit solutions are pruned.

4.3.3 Mutations. This step effectively adds additive white gaussian noise to the remaining, most-fit candidate solutions, and helps to perturb the vector such that it creates a 'mutation' effect. The magnitude of the mutation depends on the variance of the additive

noise, which is a time-decaying function that acts as an additional annealing stage.

4.3.4 Crossover Methodology. The last step is 'crossover' where the mutated set of solutions are used to repopulate the set of candidate solutions for the next iteration. The order in the spatial and temporal domain of the RIS configuration carries information about beamforming and frequency shifting respectively. The fitness function is strongly dependent on neighboring elements in the candidate solutions. Hence, to preserve the positively impacting spatio-temporal features, we use a two-point crossover methodology which retains contiguous sequences of parents. For each pair of parents, the algorithm chooses a sub-interval of the vector to crossover. For example, let the parents (a, b) and child (c) be vectors of length N. Let a randomly chosen sub-interval be (i, j). Then, the crossover operation on the parents results in a child c s.t.

$$a = [a_1, \cdots, a_i, \cdots, a_N], \quad b = [b_1, \cdots, b_j, \cdots b_N],$$
$$c = [a_1, \cdots, a_i, b_{i+1}, \cdots, b_j, a_{j+1} \cdots a_N].$$

The entire process loops over several generations until convergence. We terminate the process when the fitness of the candidate solution does not improve over the span of 500 generations and select the top performer as the optimal solution to the objective function. This process usually takes about 10,000 generations to converge and is a one-time effort prior to deployment.
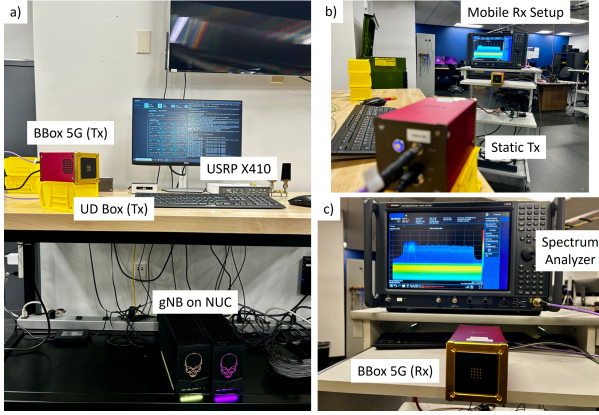
5 Evaluation

5.1 Evaluation Setup

System Configuration and Signal Generation: To validate our approach in a real-world environment, we establish a 5G communication link at 39 GHz using TMYTEK devices [40]. The setup consists of two TMYTEK UD Box 5G up/down converters, which translate an 80 MHz intermediate frequency (IF) signal centered at 2.6 GHz to the 39 GHz carrier frequency. The IF signal is a 5G-compliant waveform generated by a USRP X410 with an Open Air Interface (OAI) stack. The UD Box 5G consists of a mixer, internal local oscillator (LO), and band-pass IF and RF filters, making it well-suited for operation in the Ka-band (37–40 GHz). The signal, which comprises of synchronization (SSB), system information (SIB1), and data blocks, is visualized using a spectrum analyzer as illustrated in Fig. 9.

Phased Array and Multipath Emulation: For the evaluations, we employ the TMYTEK BBox 5G, a 4×4 phased-array antenna with 27 dB Tx/Rx gain. Each element in the array is independently configurable with a variable gain (0–6 dB) and full 360-degree phase control. To measure the effect of the multipath channel on the RIS, we configure the transmitter array with eight distinct phase settings corresponding to the space-time code deployed at the RIS and capture channel traces at a receiver where only a single array element is active. This ensures that the collected channel measurements accurately capture multipath propagation effects while incorporating the beam-steering effects of the RIS, similar to a radar scenario.

Measurement Procedure: We collected data across multiple angles (-60° to 60° in 15° increments) and distances (1 m to 4 m in 0.5 m increments) to thoroughly characterize multipath interactions in an indoor setting. To increase the density of the target locations, we interpolate the collected channel traces using splines. The experimental setup and environment are depicted in Fig. 9. The measured

Figure 9: Evaluation setup for a) transmitter, b) mobile receiver unit and indoor environment, c) close-up view of receiver connected to a spectrum analyzer

channel traces are then imported into MATLAB, where we simulate the space-time coding RIS using an FMCW waveform sweeping a 2 GHz bandwidth centered at 39 GHz, with a beam sweep duration of 100 microseconds. We supplement our indoor evaluation setup with two environments (indoor and outdoor) simulated in Wireless In-Site (WI [14]), a powerful ray-tracing tool to compute the wideband channel impulse response at millimeter wave frequencies.

RIS: The RIS in consideration is a 16×16-element, uniformly-spaced, two-dimensional array. Each RIS element is a microstrip patch-antenna modeled similar to [41] at 39 GHz in COMSOL. The resulting wideband reflection coefficient $\Gamma(f)$ and half-power beamwidth of $65°$ on Rogers RO4350B substrate are used in evaluations. Consistent with the examples from Section 3, PRISM's space-time code creates five harmonics of the fundamental frequency of 2 MHz, covering the $45°$ FoV with an angular resolution of $11°$. In the range-doppler analysis, a 2 MHz frequency-shift corresponds to a psuedo-range of 30 meters.

Baselines: We consider 3 representative baselines. For NLoS scenarios, we compare against *Metasight* [21] which employs multiple static reflectors for angular information encoding. To emulate its gray-coding scheme, we divide the field-of-view of $45°$ in 15 segments ($3°$ resolution), each with a unique combination of frequency-shifts. We also consider a static RIS with a broad-beam pattern, designed to redirect signals from targets towards the radar as illustrated in Fig. 3. Finally, for LoS scenarios, we also consider an isolated radar (no RIS) to evaluate the benefit of using a RIS either with (PRISM) or without (static RIS) angular resolution.

5.2 Non Line-of-Sight
The indoor NLoS scenario forms our main focus, thus we use channels collected from our testbed unless otherwise stated.

5.2.1 Single Target. Fig. 11a illustrates the CDF of the localization error using channels from the testbed for a single target with PRISM and two baselines. The mean error of PRISM is 31 cm while that of *Metasight* and the static RIS are 103 cm and 115 cm respectively. PRISM leads to a 3.7−fold and 3.3−fold reduction in error compared to a static RIS and *Metasight* respectively. With a static RIS unable to shift frequencies, the radar is unable to resolve the angle of incidence at the RIS, losing out on an important dimension in
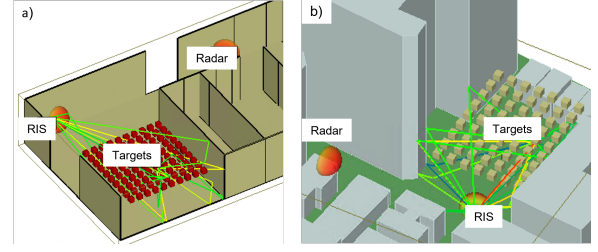
Figure 10: Additional test environments constructed in Wireless InSite for: a) indoor, b) outdoor scenarios. Multipath propagation from RIS to sample targets is illustrated.
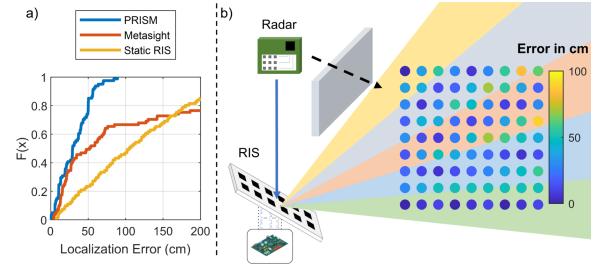
Figure 11: a) CDF of localization error for a single target in indoor scenario, b) Heatmap of error of PRISM corresponding to location (not to scale)
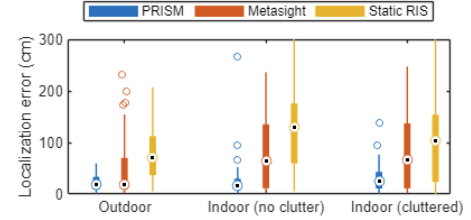
Figure 12: Box plot of localization error for different environments using the same RIS configuration

sensing. *Metasight* suffers indoors due to high multipath whereas PRISM is able to beamform to targets, thereby minimizing multipath reflections, and provide angular resolution simultaneously.

Impact of multipath: To further understand the impact of multipath on schemes that do not employ beamforming, we compare PRISM to *Metasight* in outdoor (Fig. 12a) and indoor (Fig. 12b,c) scenarios with the *same* configuration at the RIS. *Metasight* works only when there exists a singular, strong direct path between the RIS and targets. However, when there is strong multipath involved, like in NLoS indoor scenarios that is further amplified by clutter, *Metasight* fails to resolve angles accurately. Its performance substantially degrades (upper-quartile error of 150 cm), rendering it ineffective. In contrast, PRISM performs well (under 50 cm error) for both, indoor and outdoor scenarios despite having lower angular resolution ($11°$ vs $3°$), thereby providing robustness to NLoS sensing even in cluttered indoor scenarios.

Further discussion: The localization error for the target at different locations in the room is illustrated in Fig. 11b using data from the testbed. Each of the frequency-shifted beams has been illustrated as different zones in the heatmap. The primary source of error occurs on the boundaries between two zones where the
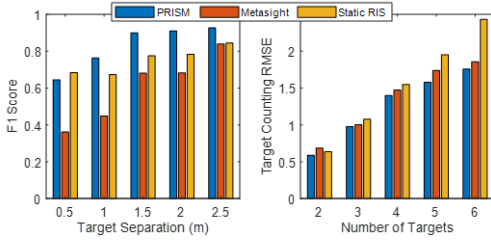
Figure 13: In NLoS scenarios, a) F1-score for resolving two targets, b) RMSE for counting several targets

algorithm incorrectly assigns the target to a neighboring angle instead. Nevertheless, the target is usually classified in a neighboring angular bin instead, thereby minimizing the localization error.

5.2.2 Multi-Target. We study PRISM's ability to detect multiple targets simultaneously in NLoS scenarios.

Two-target: First, we compare the F_1 score of detecting two targets as a function of their separation distance in Fig. 13a. PRISM obtains a detection accuracy greater than 85% (high recall) and an F_1 score greater than 0.90 at a separation of 1.5 m or more, owing to its ability to resolve targets based on both distance and angle. In contrast, static RIS can detect (albeit not localize) targets only if they do not occlude one-another and if they are at different distances, yielding an F_1 score of 0.8. *Metasight* suffers from a consistently high false-positive rate (low precision) owing to misclassification of singular targets as two-targets because of the high multipath which leads to a consistently lower F_1 score than PRISM.

N-target: Several practical applications call for detection of multiple targets (> 2) simultaneously. In Fig. 13, we observe that the target detection accuracy (normalized RMSE) is about 80% for PRISM, however the performance of a static RIS drops considerably when the number of unique targets increases, owing to its reliance solely on range based target separation, which becomes a limitation with more targets. The additional angular resolution capability leads to a significantly better performance in PRISM and *Metasight* even for larger number of targets, with PRISM having an edge over *Metasight* due to its better multipath mitigation capability.

5.3 Line-of-Sight

We show that the additional angular dimension provided by PRISM is useful for sensing multiple objects simultaneously even in LoS environments (Fig. 10b). In addition to static RIS, we also consider a radar-only baseline that can be effective in LoS. Since *Metasight*'s gray-coding framework is not directly realizable for LoS deployments, it is not considered.

We compare the accuracy of resolving two targets in Fig. 14. A typical mmWave MIMO radar [42], although has an operational range of 0.5-5m, has an angular resolution of only 30°, allowing it to distinguish two targets separated by 0.5 m only if they are placed within 1 m from the radar. From the F_1 score and RMSE of "only radar", we see that the poor angular resolution of a mmWave radar limits its use in several applications requiring a finer scale of sensing at large distances. While the static RIS is unable to provide any angular information, it provides a secondary field-of-view that augments the radar's area of detection to improve the detection performance slightly. However, it is still unable to resolve targets that are placed close together. In contrast, PRISM enables the radar
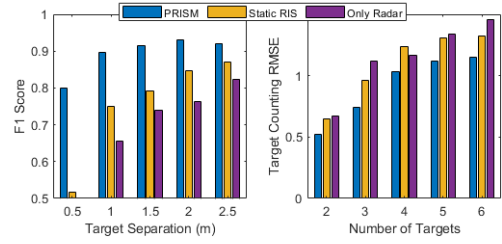

Figure 14: In LoS scenarios, a) F1-score for resolving two targets, b) RMSE for counting several targets
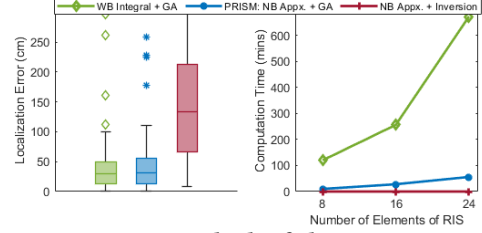

Figure 15: Comparing methods of obtaining space-time codes with: (1) localization error; (2) with computation time

to effectively leverage the higher angular resolution of RIS to yield an F_1 score over 0.9 at a separation of 1 m or more, opening the door for numerous sensing applications.

5.4 Impact of Narrowband Approximation

For the following experiment, like during practical deployment, distinct RIS configurations were computed offline on a machine (i9 @3.5 GHz, 12 cores) using the wideband integral, PRISM's narrowband approximation, and naive inversion [39] and tested in the same NLoS environment. This is a one-time computation step which is agnostic to the environment, thus making it a fixed overhead during deployment. In Fig. 15a, we see that space-time code obtained through PRISM's narrowband approximation performs just as well as the wideband integral. Furthermore, we can observe severe degradation in the performance of the space-time code obtained through naive inversion which demonstrates the utility of the genetic algorithm. However, obtaining the best space-time code incurs an exponential overhead from the wideband integral computation required in each iteration of the genetic algorithm (Fig. 15b). In contrast, PRISM's narrowband approximation reduces the computation time by 12x with only a small increase in localization error.

6 Conclusion

As mmWave sensing becomes a ubiquitous technology, enabling robust deployments in indoor settings continues to be a challenge. To this end, we proposed PRISM, a framework that brings the diversity of a passive RIS to even commodity radars through a novel spatial modulation framework that encodes angular information of targets in the frequency shifts of RIS' reflected signals. Extensive evaluations highlight PRISM's capability to deliver accurate multi-target localization capabilities even in NLoS environments, while seamlessly working with chirp-based radars.

A Appendix

LEMMA A.1. *For a random weighted-sum operation, given a vector of square-integrable functions,* $\mathbf{h}(f)$*, the complex vector which approximates it with the lowest expected error is the largest (scaled)*

eigenvector obtained through the rank-1 approximation of the auto-correlation matrix integral as defined in Equation 10.

Proof. We would like to calculate a vector, $\hat{\mathbf{h}} \in \mathbb{C}^{N \times 1}$, which approximates a vector of square-integrable functions, $\mathbf{h}(f) \in (L^2)^{N \times 1}$, with lowest expected error after a scaling operation modeled using the random vector $\mathbf{k} \in \mathbb{C}^{N \times 1}$.

$$\underset{\hat{\mathbf{h}} \in \mathbb{C}^N}{\arg \min} \mathbf{E} \left[\left| \|\hat{\mathbf{h}}\mathbf{k}^T\|^2 - \int \|\mathbf{h}(f)\mathbf{k}^T\|^2 df \right|^2 \right] \tag{8}$$

The equation further simplifies to

$$\underset{\hat{\mathbf{h}} \in \mathbb{C}^N}{\arg \min} \mathbf{E} \left[\left| \overline{\mathbf{k}}\hat{\mathbf{h}}^H \hat{\mathbf{h}}\mathbf{k}^T - \overline{\mathbf{k}} \left(\int \mathbf{h}^H(f)\mathbf{h}(f) df \right) \mathbf{k}^T \right|^2 \right]. \tag{9}$$

Let the autocorrelation matrix, $\mathbf{R} \in \mathbb{C}^{N \times N}$, be defined as $R_{ij} = \int \overline{h}_i(f) h_j(f) df$. Note $\mathbf{R}$ is Hermitian. The equation simplifies to

$$\underset{\hat{\mathbf{h}} \in \mathbb{C}^N}{\arg \min} \mathbf{E} \left[\left| \overline{\mathbf{k}} \left(\hat{\mathbf{h}}^H \hat{\mathbf{h}} - \mathbf{R} \right) \mathbf{k}^T \right|^2 \right]. \tag{10}$$

The above formulation is reminiscent of the rank-1 factorization of $\mathbf{R}$. Assuming $\mathbf{k}$ is a normally distributed random vector, it is evident that $\hat{\mathbf{h}}$ is the largest eigenvector of $\mathbf{R}$ scaled with the square-root of the largest eigenvalue.

References

[1] S. Lu, F. Liu, Y. Li, K. Zhang, H. Huang, J. Zou, X. Li, Y. Dong, F. Dong, J. Zhu, *et al.*, "Integrated sensing and communications: Recent advances and ten open challenges," *IEEE Internet of Things Journal*, vol. 11, no. 11, 2024.

[2] X. Jin, P. Zhang, C. Wan, D. Ma, and Y. Yao, "Ris assisted dual-function radar and secure communications based on frequency-shifted chirp spread spectrum index modulation," *China Communications*, vol. 20, no. 10, pp. 85–99, 2023.

[3] S. Y. Nusenu, W.-Q. Wang, and H. Chen, "Dual-function mimo radar-communications employing frequency-hopping chirp waveforms," *Progress in Electromagnetics Research M*, vol. 64, pp. 135–146, 2018.

[4] J. Zhang, R. Xi, Y. He, Y. Sun, X. Guo, W. Wang, X. Na, Y. Liu, Z. Shi, and T. Gu, "A survey of mmwave-based human sensing: Technology, platforms and applications," *IEEE Communications Surveys & Tutorials*, vol. 25, no. 4, 2023.

[5] H. Kong, C. Huang, J. Yu, and X. Shen, "A Survey of mmWave Radar-Based Sensing in Autonomous Vehicles, Smart Homes and Industry," *IEEE Communications Surveys & Tutorials*, pp. 1–1, 2024.

[6] S. Yue, H. He, P. Cao, K. Zha, M. Koizumi, and D. Katabi, "CornerRadar: RF-Based Indoor Localization Around Corners," *Proc. ACM Interact. Mob. Wearable Ubiquitous Technol.*, vol. 6, mar 2022.

[7] J. He, S. Terashima, H. Yamada, and S. Kidera, "Diffraction Signal-Based Human Recognition in Non-Line-of-Sight (NLOS) Situation for Millimeter Wave Radar," *IEEE Journal of Selected Topics in Applied Earth Observations and Remote Sensing*, vol. 14, pp. 4370–4380, 2021.

[8] G. Li, Y. Ge, Y. Wang, Q. Chen, and G. Wang, "Detection of Human Breathing in Non-Line-of-Sight Region by Using mmWave Radar," *IEEE Transactions on Instrumentation and Measurement*, vol. 71, pp. 1–11, 2022.

[9] M. Jian, G. C. Alexandropoulos, E. Basar, C. Huang, R. Liu, Y. Liu, and C. Yuen, "Reconfigurable intelligent surfaces for wireless communications: Overview of hardware designs, channel models, and estimation techniques," *Intelligent and Converged Networks*, vol. 3, no. 1, pp. 1–32, 2022.

[10] Y. Liu, X. Liu, X. Mu, T. Hou, J. Xu, M. Di Renzo, and N. Al-Dhahir, "Reconfigurable Intelligent Surfaces: Principles and Opportunities," *IEEE Communications Surveys & Tutorials*, vol. 23, no. 3, pp. 1546–1577, 2021.

[11] M. Ahmed, S. Raza, A. A. Soofi, F. Khan, W. U. Khan, S. Z. U. Abideen, F. Xu, and Z. Han, "Active Reconfigurable Intelligent Surfaces: Expanding the Frontiers of Wireless Communication-A Survey," *IEEE Comm Surveys & Tutorials*, 2024.

[12] M. A. ElMossallamy, H. Zhang, L. Song, K. G. Seddik, Z. Han, and G. Y. Li, "Reconfigurable intelligent surfaces for wireless communications: Principles, challenges, and opportunities," *IEEE Transactions on Cognitive Communications and Networking*, vol. 6, no. 3, pp. 990–1002, 2020.

[13] "OpenAirInterface." https://openairinterface.org/.

[14] "Wireless InSite®, Remcom Inc." https://www.remcom.com/.

[15] M. Gustafsson, A. Andersson, T. Johansson, S. Nilsson, A. Sume, and A. Orbom, "Extraction of Human Micro-Doppler Signature in an Urban Environment Using a "Sensing-Behind-the-Corner" Radar," *IEEE Geoscience and Remote Sensing Letters*, vol. 13, no. 2, pp. 187–191, 2016.

[16] T. Johansson, A. Andersson, M. Gustafsson, and S. Nilsson, "Positioning of moving non-line-of-sight targets behind a corner," in *2016 European Radar Conference (EuRAD)*, pp. 181–184, 2016.

[17] W. Chen, H. Yang, X. Bi, R. Zheng, F. Zhang, P. Bao, Z. Chang, X. Ma, and D. Zhang, "Environment-aware Multi-person Tracking in Indoor Environments with MmWave Radars," *Proc. ACM Interact. Mob. Wearable Ubiquitous Technol.*, vol. 7, sep 2023.

[18] S. Wei, J. Wei, X. Liu, M. Wang, S. Liu, F. Fan, X. Zhang, J. Shi, and G. Cui, "Nonline-of-sight 3-D imaging using millimeter-wave radar," *IEEE Transactions on Geoscience and Remote Sensing*, vol. 60, pp. 1–18, 2021.

[19] L. Dodds, H. Shanbhag, J. Guan, S. Gupta, and H. Hassanieh, "Around the corner mmwave imaging in practical environments," in *Proceedings of the 30th Annual International Conference on Mobile Computing and Networking*, ACM MobiCom '24, (New York, NY, USA), p. 953–967, Association for Computing Machinery, 2024.

[20] N. Scheiner, F. Kraus, F. Wei, B. Phan, F. Mannan, N. Appenrodt, W. Ritter, J. Dickmann, K. Dietmayer, B. Sick, *et al.*, "Seeing around street corners: Non-line-of-sight detection and tracking in-the-wild using doppler radar," in *Proceedings of the IEEE/CVF Conference on Computer Vision and Pattern Recognition*, 2020.

[21] T. Woodford, K. Qian, and X. Zhang, "Metasight: High-Resolution NLoS Radar with Efficient Metasurface Encoding," in *Proceedings of the 21st ACM Conference on Embedded Networked Sensor Systems*, SenSys '23, (New York, NY, USA), p. 308–321, Association for Computing Machinery, 2024.

[22] A. Aubry, A. De Maio, and M. Rosamilia, "RIS-Aided Radar Sensing in N-LOS Environment," in *2021 IEEE 8th International Workshop on Metrology for AeroSpace (MetroAeroSpace)*, pp. 277–282, 2021.

[23] K. Chen, C. Qi, O. A. Dobre, and G. Y. Li, "Simultaneous beam training and target sensing in isac systems with ris," *IEEE Tran on Wireless Communications*, 2023.

[24] M. Rihan, E. Grossi, L. Venturino, and S. Buzzi, "Spatial diversity in radar detection via active reconfigurable intelligent surfaces," *IEEE Signal Processing Letters*, vol. 29, pp. 1242–1246, 2022.

[25] A. Bazzi and M. Chafii, "RIS-Enabled Passive Radar towards Target Localization," 2022.

[26] R. P. Sankar, B. Deepak, and S. P. Chepuri, "Joint communication and radar sensing with reconfigurable intelligent surfaces," in *2021 IEEE 22nd International Workshop on Signal Processing Advances in Wireless Communications (SPAWC)*, pp. 471–475, IEEE, 2021.

[27] Z. Liu, H. Zhang, T. Huang, F. Xu, and Y. C. Eldar, "Hybrid RIS-assisted MIMO dual-function radar-communication system," *IEEE Tran on Signal Processing*, 2024.

[28] X. Wang, Z. Fei, Z. Zheng, and J. Guo, "Joint Waveform Design and Passive Beamforming for RIS-Assisted Dual-Functional Radar-Communication System," *IEEE Transactions on Vehicular Technology*, vol. 70, no. 5, pp. 5131–5136, 2021.

[29] S. Buzzi, E. Grossi, M. Lops, and L. Venturino, "Foundations of MIMO Radar Detection Aided by Reconfigurable Intelligent Surfaces," *IEEE Transactions on Signal Processing*, vol. 70, pp. 1749–1763, 2022.

[30] Y. He, Y. Cai, H. Mao, and G. Yu, "RIS-assisted communication radar coexistence: Joint beamforming design and analysis," *IEEE Journal on Selected Areas in Communications*, vol. 40, no. 7, pp. 2131–2145, 2022.

[31] A. G. Stove, "Linear FMCW radar techniques," in *IEE Proceedings F (Radar and Signal Processing)*, vol. 139, pp. 343–350, IET, 1992.

[32] S. Rao, "Introduction to mmWave sensing: FMCW radars," *Texas Instruments (TI) mmWave Training Series*, pp. 1–11, 2017.

[33] R. Wang, Y. Yang, B. Makki, and A. Shamim, "A wideband reconfigurable intelligent surface for 5g millimeter-wave applications," *IEEE Transactions on Antennas and Propagation*, vol. 72, no. 3, pp. 2399–2410, 2024.

[34] J. Zhang, Z. Li, and Z. Zhang, "Wideband active riss: Architecture, modeling, and beamforming design," *IEEE Communications Letters*, vol. 27, no. 7, 2023.

[35] W. Yan, W. Hao, C. Huang, G. Sun, O. Muta, H. Gacanin, and C. Yuen, "Beamforming analysis and design for wideband thz reconfigurable intelligent surface communications," *IEEE Journal on Selected Areas in Communications*, 2023.

[36] M. Saikia, K. V. Srivastava, and S. A. Ramakrishna, "Frequency-shifted reflection of electromagnetic waves using a time-modulated active tunable frequency-selective surface," *IEEE Transactions on Antennas and Propagation*, vol. 68, no. 4, pp. 2937–2944, 2020.

[37] L. Zhang, X. Q. Chen, S. Liu, Q. Zhang, J. Zhao, J. Y. Dai, G. D. Bai, X. Wan, Q. Cheng, G. Castaldi, *et al.*, "Space-time-coding digital metasurfaces," *Nature communications*, vol. 9, no. 1, p. 4334, 2018.

[38] R. M. McLeod, *The generalized Riemann integral*, vol. 20. American Mathematical Soc., 1980.

[39] J. C. A. Barata and M. S. Hussein, "The Moore–Penrose pseudoinverse: A tutorial review of the theory," *Brazilian Journal of Physics*, vol. 42, pp. 146–165, 2012.

[40] "TYM Technology Inc." https://tmytek.com/.

[41] X. Tan, Z. Sun, D. Koutsonikolas, and J. M. Jornet, "Enabling Indoor Mobile Millimeter-wave Networks Based on Smart Reflect-arrays," in *IEEE INFOCOM 2018 - IEEE Conference on Computer Communications*, pp. 270–278, 2018.

[42] "AWR6843ISK Evaluation Board, Texas Instruments Incorporated." https://www.ti.com/tool/AWR6843ISK.